Research Article | Vol. 25, No. 25 | 11 Dec 2017 | OPTICS EXPRESS 31840
Optics EXPRESS

Polycapillary-boosted instrument performance in the extreme ultraviolet regime for inverse photoemission spectroscopy

CHRISTOPH BRAIG,[1,2,3,*] ANDREY SOKOLOV,[2] REGAN G. WILKS,[3,4] XENIYA KOZINA,[3] THOMAS KUNZE,[3] SEMPFIRA BJEOUMIKHOVA,[5] MARKUS THIEL,[5] ALEXEI ERKO,[2] AND MARCUS BÄR[3,4,6]

[1]*Institut für Angewandte Photonik e.V., Rudower Chaussee 29/31, 12489 Berlin, Germany*
[2]*Department for Nanometer Optics and Technology, Helmholtz-Zentrum Berlin für Materialien und Energie, Albert-Einstein-Str. 15, 12489 Berlin, Germany*
[3]*Renewable Energy, Helmholtz-Zentrum Berlin für Materialien und Energie, Hahn-Meitner-Platz 1, 14109 Berlin, Germany*
[4]*Energy Materials In-Situ Laboratory Berlin (EMIL), Albert-Einstein-Str. 15, 12489 Berlin, Germany*
[5]*Helmut Fischer GmbH, Rudower Chaussee 29/31, 12489 Berlin, Germany*
[6]*Institut für Physik, Brandenburgische Technische Universität Cottbus-Senftenberg, Platz der Deutschen Einheit 1, 03046 Cottbus, Germany*
[*]*braig@iap-adlershof.de*

Abstract: A collimating polycapillary half lens, traditionally used in the medium and hard X-ray band, is operated at a photon energy of 36 eV for the first time. While the transmission still exceeds 50%, the measured and simulated spatial resolution and angular divergence approach 0.4 mm or less and at most 20 mrad, respectively. This unexpected, superior performance of the polycapillary optic in the extreme Ultraviolet could enable the design of an efficient, versatile and compact spectrometer for inverse photoemission spectroscopy (IPES): Its wavelength-dispersive component, a customized reflection zone plate, can maintain an energy resolution of 0.3 eV, whereas the sensitivity may be enhanced by more than one order of magnitude, compared to conventional spectrometers. Furthermore, the overall length of 0.9 m would allow for an eased alignment and evacuation. We see a significant potential for numerous polycapillary-based XUV / soft X-ray instruments in the future, in particular after further optimization for this long wavelength regime.

OCIS codes: (050.1950) Diffraction gratings; (120.1680) Collimation; (120.3620) Lens system design; (300.6190) Spectrometers; (340.7480) X-rays, soft x-rays, extreme ultraviolet (EUV).

References and links

1. L. Kipp, M. Boehme, H. Carstensen, R. Claessen, and M. Skibowski, "Compact grating spectrometer for inverse photoemission spectroscopy," Rev. Sci. Instr. **68**, 2144—2148 (1997).
2. M. Bär, B.-A. Schubert, B. Marsen, R. G. Wilks, S. Pookpanratana, M. Blum, S. Krause, T. Unold, W. Yang, L. Weinhardt, C. Heske, and H.-W. Schock, "Cliff-like conduction band offset and KCN-induced recombination barrier enhancement at the CdS/Cu2ZnSnS4 thin-film solar cell heterojunction," Appl. Phys. Lett. **99**, 222105 (2011).
3. J. Metje, M. Borgwardt, A. Moguilevski, A. Kothe, N. Engel, M. Wilke, R. Al-Obaidi, D. Tolksdorf, A. Firsov, M. Brzhezinskaya, A. Erko, I. Y. Kiyan, and E. F. Aziz, "Monochromatization of femtosecond XUV light pulses with the use of reflection zone plates," Opt. Express **22**, 10747—10760 (2014).
4. X. Zeng, F. Duewer, M. Feser, C. Huang, A. Lyon, A. Tkachuk, and W. Yun, "Ellipsoidal and parabolic glass capillaries as condensers for x-ray microscopes," Appl. Opt. **47**, 2376—2381 (2008).
5. C. A. MacDonald, "Focusing Polycapillary Optics and Their Applications," X-Ray Opt. Instrum. **2010**, 867049 (2010).
6. F. Schäfers, P. Bischoff, F. Eggenstein, A. Erko, A. Gaupp, S. Künstner, M. Mast, J.-S. Schmidt, F. Senf, F. Siewert, A. Sokolov, and T. Zeschke, "The At-Wavelength Metrology Facility for UV- and XUV-Reflection and Diffraction Optics at BESSY-II," J. Synchr. Rad. **23**, 67–77 (2016).

#304316 https://doi.org/10.1364/OE.25.031840
Journal © 2017 Received 7 Aug 2017; revised 14 Nov 2017; accepted 27 Nov 2017; published 7 Dec 2017

Optics EXPRESS

7. A. Sokolov, P. Bischoff, F. Eggenstein, A. Erko, A. Gaupp, S. Künstner, M. Mast, J.-S. Schmidt, F. Senf, F. Siewert, T. Zeschke, and F. Schäfers, "At-wavelength metrology facility for soft X-ray reflection optics," Rev. Sci. Instrum. **87**, 052005 (2016).
8. W. H. Richardson, "Bayesian-Based Iterative Method of Image Restoration," J. Opt. Soc. Am. **62**, 55—59 (1972).
9. L. B. Lucy, "An iterative technique for the rectification of observed distributions," Astron. J. **79**, 745-–754 (1974).
10. Optica Software, 613 W Delaware Ave, Urbana IL, 61801, USA, http://www.opticasoftware.com (2017).
11. A. Liu, "Simulation of X-ray beam collimation by polycapillaries," Nucl. Instr. Meth. Phys. Res. B **234**, 555-–562 (2005).
12. A. Snigirev, A. Bjeoumikhov, A. Erko, I. Snigireva, M. Grigoriev, V. Yunkin, M. Erko, and S. Bjeoumikhova, "Two-step hard X-ray focusing combining Fresnel zone plate and single-bounce ellipsoidal capillary," J. Synchr. Rad. **14**, 326—330 (2007).
13. B. L. Henke, E. M. Gullikson, and J. C. Davis, "X-ray interactions: photoabsorption, scattering, transmission, and reflection at E = 50 – 30000 eV, Z = 1 – 92," At. Data Nucl. Data Tables **54**, 181—342 (1993).
14. L. Kaihola, "Anomalous Soft X-Ray Reflectivity of Borosilicate Glass by Successive Grazing Reflections," Phys. Stat. Sol. A **65**, 163—166 (1981).
15. D. H. Bilderback, S. A. Hoffman, and D. J. Thiel, "Nanometer Spatial Resolution Achieved in Hard X-ray Imaging and Laue Diffraction Experiments," Science **263**, 201—203 (1994).
16. L. Vincze, K. Janssens, F. Adams, A. Rindby, and P. Engström, "Interpretation of capillary generated spatial and angular distributions of x rays: Theoretical modeling and experimental verification using the European Synchrotron Radiation Facility Optical beam line," Rev. Sci. Instr. **69**, 3494-–3503 (1998).
17. T. Sun, Z. Liu, Y. Li, X. Lin, P. Luo, Q. Pan, and X. Ding, "Fine structures of divergence of polycapillary X-ray optics," Nucl. Instr. Meth. Phys. Res. B **269**, 2758-– 2761 (2011).
18. T. Sun and C. A. MacDonald, "Full-field transmission x-ray imaging with confocal polycapillary x-ray optics," J. Appl. Phys. **113**, 053104 (2013).
19. S. H. Nowak, M. Petric, J. Buchriegler, A. Bjeoumikhov, Z. Bjeoumikhov, J. von Borany, F. Munnik, M. Radtke, A. D. Renno, U. Reinholz, O. Scharf, J. Tilgner, and R. Wedell, "Road to micron resolution with a color X-ray camera–polycapillary optics characterization," arXiv:1705.08939 [physics.ins-det].
20. H. Löchel, C. Braig, M. Brzhezinskaya, F. Siewert, P. Baumgärtel, A. Firsov, and A. Erko, "Femtosecond high-resolution hard X-ray spectroscopy using reflection zone plates," Opt. Express **23**, 8788-–8799 (2015).
21. J. I. Larruquert, L. V. Rodríguez-de Marcos, J. A. Méndez, P. J. Martin, and A. Bendavid, "High reflectance ta-C coatings in the extreme ultraviolet," Opt. Express **21**, 27537—27549 (2013).

1. Introduction

Inverse photoemission spectroscopy (IPES) provides access to the unoccupied density of states. Depending on the injection of electrons of fixed or variable energy, the emitted photons may be either recorded over an extended range in the spectrometric or – now at a specified wavelength – in the isochromatic mode [1, 2]. Low count rates, being typical for that technique, demand an optimized instrumental sensitivity without losing the spectral resolution capabilities. Especially in the XUV- and x-ray range, reflection zone plates (RZPs) as "all-in-one" dispersive and focusing optics may help to realize these properties with minimized complexity [3].

However, the antagonism between the efficiency-related étendue under which the photons are collected and the achievable resolution would imply not only a meter-sized source-detector distance but impracticably large grating dimensions as well.

Hence, our work suggests to grasp and collimate the sample emission by a polycapillary half lens (PCL) [4, 5], to exploit and enhance the advantages of the customized RZP. The paper is organized as follows: In Sect. 2, we present experiments which characterize the PCL at an energy of 36 eV. The data are compared to simulations in Sect. 3. Based on these empirical findings for the PCL behavior, we sketch in Sect. 4 a possible instrumental design for a potential, future IPES spectrometer at 36 eV and study an extension of its range of use to a wide energy range in Sect. 5. In conclusion, Sect. 6 discusses both the specific experimental results for the PCL and the induced, but so far only calculated performance of the planned spectrometer.

2. Experimental characterization of the polycapillary half lens

The micron sized borosilicate glass tubes of the employed monolithic PCL, 36.2 mm in length, are tapered from the wide and nearly parallel "outer" aperture toward the "inner" focusing

Optics EXPRESS

end as depicted in Fig. 1. A quasi monochromatic, nearly parallel beam with a residual

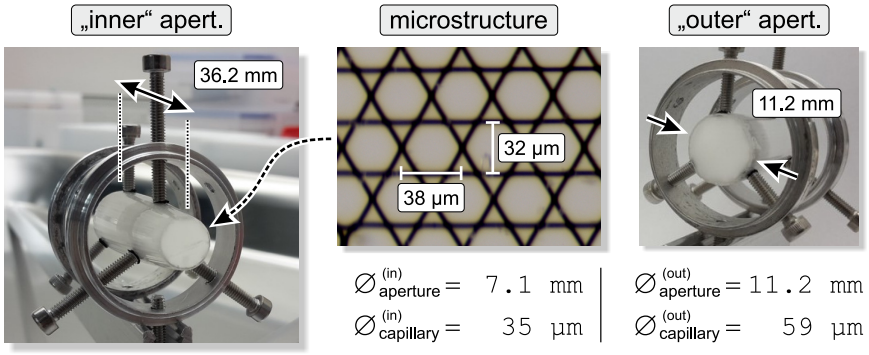

Fig. 1. Shape of the PCL and its microscopic structure. Scales are indicated for both ends.

divergence of 3.0 mrad × 0.5 mrad and two lateral dimension modes – given by a cross section of 0.20 mm × 0.36 mm (H × V) or 0.7 mm × 4.9 mm (H × V) – is used to test the PCL in its focusing configuration at the reflectometry end station of the optics beamline at the electron storage ring BESSY II [6, 7], as illustrated in Fig. 2. The scan across the lens diameter with an

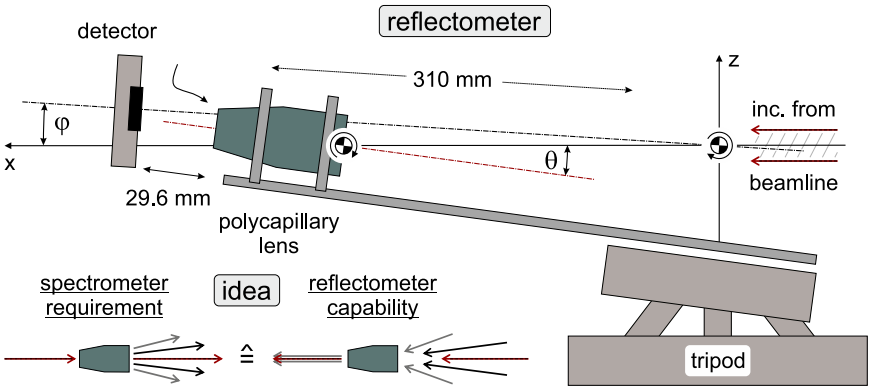

Fig. 2. Scheme of the experimental setup to test the PCL. As opposed to the later use in spectrometry (inset in the lower left corner), the PCL is mounted on a tripod stage with a prolongation arm to measure the focal intensity distribution for tilt angles θ. The detector is rotated independently by an angle φ on a radius of 310 mm around $\vec{r} = 0$ (center of mass symbols).

0.1 mm wide exit slit in steps of 0.2 mm, shown in Fig. 3, reveals a roughly uniform transmission in both lateral dimensions (y, z), averaged to $\langle T \rangle_{\Delta z} = 53.3\%$ over an open aperture of 10.7 mm, 4.4% less than the nominal optical diameter $\varnothing^{(\mathrm{out})}_{\mathrm{aperture}}$. Prior further characterization, the PCL is annealed (for cleaning). Despite this procedure, which can even increase the mean transmission to about 60%, the porous surface is likely still contaminated by residual dust that may cause the transmission variation.

The tripod mounting allows to rotate the PCL by an angle $-1° \le \theta \le +1°$ with respect to the incident beam and – independently around the y-axis – the detector in the focal plane by $-0.3° \le \varphi \le +0.3°$ (Fig. 2). This scheme is used to probe the focus shape for the on-axis ($\theta = 0°$) and tilted (e.g. $\theta = 0.5°$) orientations of the PCL. The beam is approximately centered to the

Optics EXPRESS

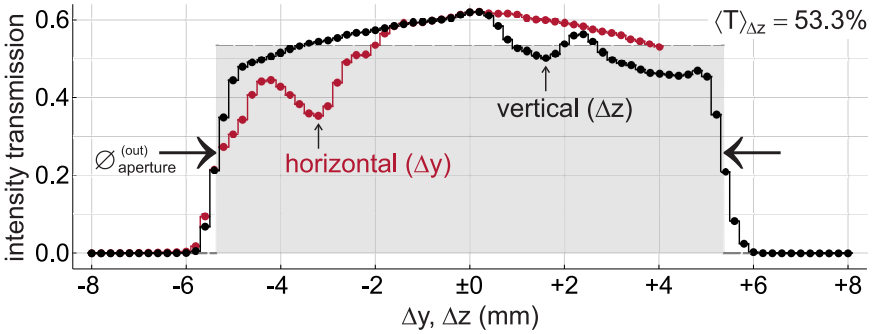

Fig. 3. PCL transmission profile, measured in horizontal (red, incomplete recording of data) and vertical (black) direction across the output aperture. The gray area represents the equivalent for uniform transmission at $\langle T \rangle_{\Delta z} = 53.3\%$ over the empirical width of 10.7 mm, which differs from the nominal diameter by less than 5%.

optical axis of the PCL and its size is adjusted to 0.7 mm × 4.9 mm (H × V). For a fixed setting of θ, the position of the GaAsP photodiode (Hamamatsu G1127-02), the active area (surface) of which is masked by a pinhole of 0.10 mm in diameter, is scanned in steps of 0.05 mm to generate the raw data set. An iterative Richardson-Lucy algorithm [8, 9] is subsequently applied to deconvolve the Gaussian point spread function with an FWHM ("full width at half maximum") of 0.11 mm from the actual intensity distribution. Two representative results are shown in Fig. 4. The 2D mapping shows a well-confined on-axis focus, which transforms into an annulus of

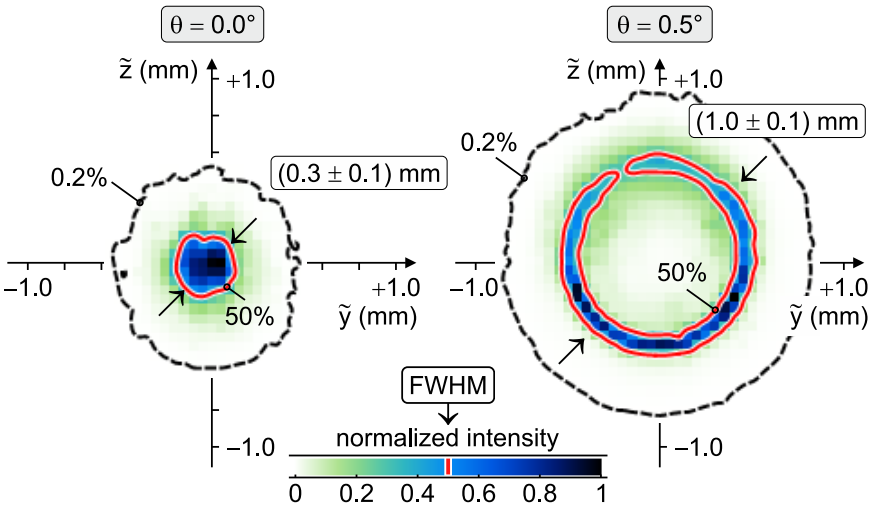

Fig. 4. Typical examples of recorded focal intensity patterns, generated by the PCL at 36 eV under on-axis illumination ($\theta = 0.0°$) on the left and in tilted orientation ($\theta = 0.5°$) on the right. Diagonal arrows characterize in local detector coordinates $(\tilde{y}, \tilde{z})$ the lateral size corresponding to w_θ in the former and $2r_\theta$ in the latter case, see Eq. (1). Contours at the 50% (red) and 0.2% (black dashed) level illustrate FWHM and scattering, respectively.

reproducible circular symmetry in the off-axis case. Other 2D patterns, which are not shown but have been taken under comparable or at least similar conditions, are characterized by a variability in the order of ±0.1 mm with respect to this spot size or ring width parameter, respectively. Such

an uncertainty might be either caused by a slight misalignment of the PCL, to which this kind of optics is known to be quite sensitive, or slightly different experimental circumstances.

In general, the pattern $I_\theta(\tilde{r})$ is modeled approximately as

$$I_\theta(\tilde{r}) \approx a_\theta(1 + b_\theta \tilde{z}^3)\exp[-4\ln 2(w_\theta^{-2}(\tilde{r} - r_\theta))^2] \quad \text{with} \quad \tilde{r}^2 \equiv \tilde{y}^2 + \tilde{z}^2 \tag{1}$$

and parameters indexed by θ. We define the outer diameter $\varnothing_{\text{focus}}^{(\text{cap.})}(\theta) \equiv 2r_\theta + w_\theta$ for the ring on the right of Fig. 4, such that for $r_\theta \to 0$ the width w_θ may be conveniently identified with the "focal spot size" (FWHM), being used under on-axis illumination on the left side.

To establish a systematic and reliable relation for $\varnothing_{\text{focus}}^{(\text{cap.})}(\theta)$, we make a more refined measurement set for a series of tilt angles of the focal plane along the $\tilde{z}$-axis – with a narrow beam of only 0.20 mm × 0.36 mm (H × V) in size. In addition, the signal is either detected by an 0.14 mm wide slit or a pinhole of 0.10 mm in diameter. Both apertures yield, within the limits of empirical variability, consistent results for $\int_{-\infty}^{+\infty} I_\theta(\tilde{r})d\tilde{y}$ and $I_\theta(\tilde{y} = 0, \tilde{z})$, respectively. After deconvolution of the 1D intensity data [8,9], the function from Eq. (1) is used once again to extract the θ-related parameters from each fit with an averaged accuracy of (13 ± 3)%. The data from the pinhole probe are summarized in Fig. 5, together with the mean spot size $\varnothing_{\text{focus}}^{(\text{cap.})}(0)$ from the slit and pinhole scan including its uncertainty. An asymptotic linearity with $d\varnothing_{\text{focus}}^{(\text{cap.})}/d\theta = 1.71$ mm/deg dominates

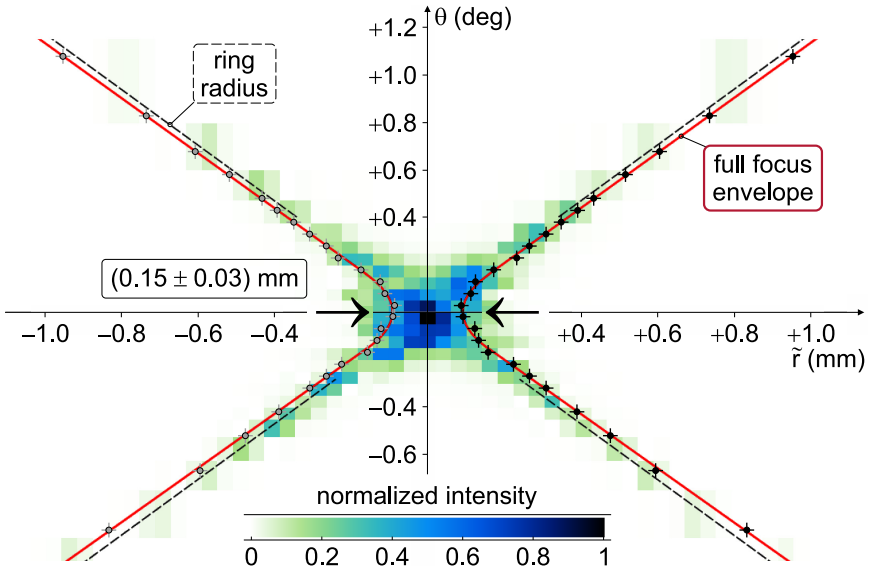

Fig. 5. Radial intensity distribution in the focal plane for tilts $-1° \le \theta \le +1°$, scanned by an 0.1 mm wide pinhole (color code). The annular patterns peak on the "ring radius" r_θ (black dashed lines). Measured / mirrored (black / gray dots) and fitted (red) data define the "full focus envelope" $2r_\theta + w_\theta$.

beyond $|\theta| \gtrsim 0.2°$, whereas the least squares fit around $\varnothing_{\text{focus}}^{(\text{cap.})}(0) = (0.15 \pm 0.03)$ mm implies an angular tolerance of $|\theta| \le 0.07°$ within which the spot expands by no more than 20%. On the other hand, the overall spot size minimum from Fig. 5 is found in a focal distance $F = 29.6$ mm from the inner aperture of the PCL, as sketched in Fig. 2. In the Gaussian beam approximation, the associated axial depth of field (DOF) is given by the Rayleigh length $\Delta x_R = \pm 1.3$ mm for the associated narrow beam. If enlarged to 0.7 mm × 4.9 mm (H × V), the beam generates an accordingly increased DOF of ±1.9 mm. While the longitudinal tolerance for on-axis focusing benefits from that growth, the sensitivity to the ring diameter in the tilted case remains: For

instance, the detector plane was possibly defocused by +1.5 mm when some enlarged annular patterns such as the one on the right in Fig. 4 were recorded.

3. Comparison to polycapillary ray tracing

An elementary 3D ray tracing simulation [10], based on the known PCL geometry [11], is performed for an ellipsoidal, mirror-like capillary assembly [12]. Its differential reflectivity $dR/d\theta \approx -0.06/\text{deg}$ [13, 14], together with an assumed surface roughness of 3 nm (rms), leads primarily to an angular dependence of the transmission – exponentiated to $R^n(\theta)$ by n-fold multiple reflection – and a slight broadening of the annular width w_θ. The glass surface properties have an only marginal effect on the image forming process.

Considering one straight, i.e. the central capillary at first, our simple scheme rather unveils how the hollow tapered tube [15] generates from an incident, parallel (but tilted) beam at the inner aperture the typical light cone [16] which propagates toward the focal plane. Its opening angle almost perfectly agrees (> 95%) with the observed spread $2r_\theta/F$ (see Fig. 5) over the considered range $-1^\circ \le \theta \le +1^\circ$ and the cone's blur, i.e., the simulated analogue to the measured quantity w_θ, corresponds to an estimated slope error of ~ 1 arcsec for the borosilicate surface along the propagation distance inside the PCL.

However, the vast amount of more or less curved channels in the real device significantly determines the blur of the detected intensity distribution, since the number of reflections and hence the angular spread of the emitted beam increases from the optical axis toward the outer regions of the PCL aperture. This phenomenon became already manifest in the different experimental results for the focal spot size under variable illumination, as shown in Fig. 4 and Fig. 5. Extensive simulations confirm both the aperture dependence of the on-axis spatial resolution as well as a widely scattered, though relatively weak background across off-axis annular patterns, that nearly vanishes toward larger angles $|\theta| \lesssim 1^\circ$. Indeed, the findings from the 2D recordings with the medium-sized beam as depicted in Fig. 4 can be verified in terms of $\varnothing^{(\text{cap.})}_{\text{focus}}(0) \approx 0.24$ mm and $w_\theta = (0.13 \pm 0.01)$ mm.

In order to provide a realistic basis for the expected performance and practical usage of the PCL, we trace in a third and final step its modeled version over randomly selected channels within the full aperture diameter of 11.2 mm. Figure 6 depicts exemplarily a few pixelated ray footprints out of the complete series of 25 simulations across the θ range. While the simulated

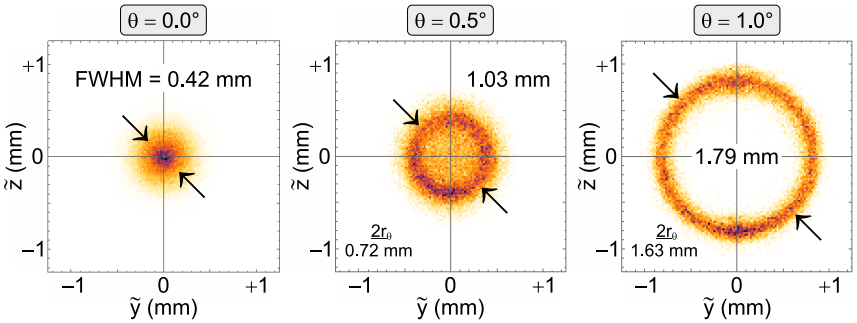

Fig. 6. Simulated focal intensity pattern for tilt angles θ up to 1.0°, using an incident beam of 11.2 mm in diameter ("full aperture"). The diagonal arrows denote the FWHM and outer annular dimension $2r_\theta + w_\theta$, respectively. The net ring diameter is given in the left lower corner. Each plot is composed from the output of ≈ 150 randomly distributed capillaries.

ring diameter $2r_\theta$ for $\theta \neq 0^\circ$ well confirms the measured findings shown in Fig. 5, the on-axis spot size w_θ on the left of Fig. 6 exceeds the experimental results from the 2D (Fig. 4) and 1D

(Fig. 5) scans. In the off-axis case, $w_\theta = (0.3 \pm 0.1)$ mm also lies above the corresponding values for partial illumination from above. The overall ring-shaped distribution is nonetheless almost unchanged toward $|\theta| \to 1°$.

Since this scenario could not be verified in the reflectometer (Sect. 2) due to technical constraints, its implications on the spectrometer behavior should be considered as an, albeit well-founded, prediction. The following analysis is hence based on the simulations from Fig. 6 which rely on extrapolated experimental data. Within the error margins of this study, that inevitable uncertainty affects the energy resolution and sensitivity to an only low extent, as we will see in Sect. 4.

In the on-axis focusing mode, the divergence $\Delta\beta^{(i)}_{cap.}$ – defined as the angular FWHM over the emitted bundle of rays from a single capillary [5] – is related to the spatial resolution via

$$\varnothing^{(cap.)}_{focus} = \sqrt{[\varnothing^{(in)}_{cap.}]^2 + [F \cdot \Delta\beta^{(i)}_{cap.}]^2} \;\Rightarrow\; \Delta\beta^{(i)}_{cap.} = (10 \pm 4)\,\text{mrad} \tag{2}$$

for the measured and simulated focal widths from Figs. 4–6, respectively. Such values are not only of comparable magnitude as the critical angle $\theta_{crit.}$ for total external reflection of medium and hard x-rays on borosilicate glass [5], but also at least $13\times$ smaller than $\theta_{crit.}$ for the photon energy of 36 eV [13] used in our experiments – a result that might augment published theory [5, 17–19].

4. Design of the IPES detector

To exploit these optical features for the construction of a future IPES instrument, we will rather operate the PCL in the reversed, collimating mode [4], as sketched in the inset of Fig. 2. In this scheme, the PCL should capture a certain fraction from the sample emission of width $\varnothing^{(1)}_{src.}$, which is located in the focal plane and will be hence denoted in the following as the "primary" or real source. The clue to find this actually gathered part of the emitted radiation relies on the sufficiently bounded distribution $I_\theta(\tilde{r})$ in Figs. 4–6, i.e. the spots or annuli to which the photons were initially focused. Besides, the integrated and normalized transmitted power $\mathcal{P}_\theta = 2\pi \int I_\theta(\tilde{r})\tilde{r}d\tilde{r}$ to the focal pattern declines with $|\theta|$ or, equivalently, the capture efficiency drops toward larger radii in the sample plane, according to the left plot in Fig. 7. The function $I_\theta(\tilde{r})$ hence probes and

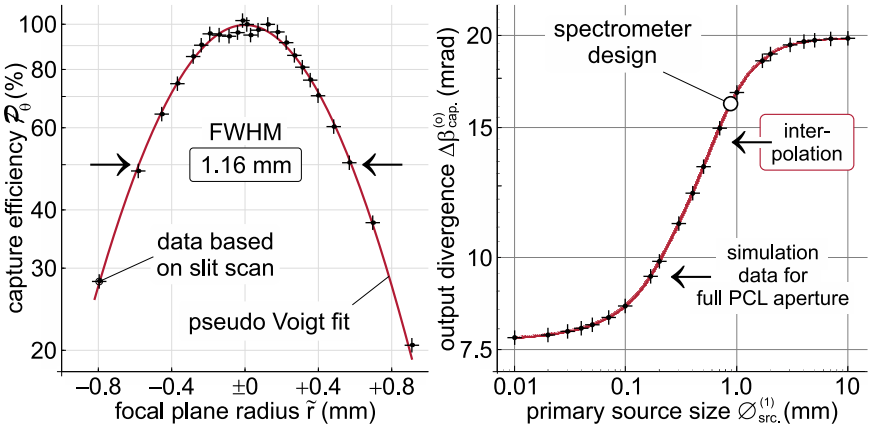

Fig. 7. Capture efficiency (=totally detected power) as a function of the radial focal plane coordinate $\tilde{r}$ (see Fig. 5) on the left and estimated output beam divergence for a Gaussian primary source of $\varnothing^{(1)}_{src.}$ (FWHM) in size on the right. The data (+) and their interpolated function (red curve) refer to the simulation from Fig. 6 in the ray-traced full aperture limit. The spectrometer is designed with $\Delta\beta^{(o)}_{cap.} = 16$ mrad.

Optics EXPRESS

weights the Gaussian primary source continuously over the emission region. An upper bound to its effective area – or its lateral size $\varnothing^{(c.)}_{src.}$ – from where the PCL may collect photons is expected near the FWHM of $\mathcal{P}_\theta$, denoted in Fig. 7. Table 1 lists the values of the calculated size of captured emission area in relation to the lateral size of a real source. At the outer aperture of

Table 1. **Captured emission (FWHM) from primary source**

$\varnothing^{(1)}_{src.}$ [mm]	0.01	0.10	0.15	0.30	0.50	0.80	1.00	1.50	2.00	3.00	10.0
$\varnothing^{(c.)}_{src.}$ [mm]	0.01	0.10	0.15	0.29	0.46	0.65	0.75	0.91	0.99	1.07	1.15

the PCL, the captured radiation from the radial range within $r_\theta \pm w_\theta/2$ is re-emitted to a hollow cone, characterized by an opening angle 2θ, such that the θ-weighted sum defines the angular output divergence $\Delta\beta^{(o)}_{cap.}(\varnothing^{(1)}_{src.})$ for an extended emission region, as it is evaluated on the right in Fig. 7. We consider the simulated experiment for the full illumination of the PCL with the circular beam as specified in Sect. 3: In the limit of a point source, the residual spread confines the nearly parallel beam to no more than 8 mrad; and a widely distributed emission should experience an up to 2.5 × worse collimation, respectively. Compared to the experiment using the medium-sized (0.7 mm × 4.9 mm) rectangular beam, the effect of this full illumination on the divergence characteristics is marginal for sources which are larger than about 0.2 mm. Since a source of $\sim 10^{-1}$ mm in size is only feasible by means of an undesired pinhole which would reduce the photon flux, the red curve marks effectively the practical upper limit ("worst case") to the output divergence of the PCL.

In our projected IPES instrument an electron beam (in this case a Kimball Physics ELG-2A electron gun as an electron source is used) will be focused on a sample surface resulting in a mm-size or larger emission area; and in analogy to the quantum mechanical position momentum product, the uncertainty and hence spectral blur due to that wide emission area $A^{(1)}_{src.}$ is overcompensated by the small solid angle $\Omega^{(o)}_{cap.}$ of the collimated beam. The lossless étendue

$$A^{(1)}_{src.} \times \Omega^{(o)}_{cap.} = [\pi\, \varnothing^{(c.)}_{src.}(\varnothing^{(1)}_{src.}) \sin(\Delta\beta^{(o)}_{cap.}(\varnothing^{(1)}_{src.})/4)]^2, \tag{3}$$

an intrinsic feature of the PCL, should be nonetheless kept minimal via $\varnothing^{(1)}_{src.}$ (Tab. 2), in agreement with the technical and scientific needs. As shown in Fig. 8, the sample-grating distance R'_1 can be

Table 2. **Lossless captured étendue (Eq. 3) in units of $[\mu m^2]$**

$\varnothing^{(1)}_{src.}$ [mm]	0.01	0.10	0.15	0.50	1.00	1.50	10.0
$A^{(1)}_{src.} \times \Omega^{(o)}_{cap.}$	4×10^{-3}	5×10^{-1}	$1 \times 10^{\pm 0}$	$2 \times 10^{+1}$	$1 \times 10^{+2}$	$2 \times 10^{+2}$	$3 \times 10^{+2}$

shortened in this way, while the performance of the spectrometer is maintained or even improved: If matched to the PCL-based setup in respect of its étendue by a suitably adjusted size and position of the virtual source, the polycapillary-free, conventional analogue with an elongated entrance arm R_1 provides the same dispersion and spatial resolution in the common detection plane, but a strongly reduced acceptance angle – and thus a diminished fraction of the radiation from the sample can be collected by the grating. At the design energy $E_0 = 36$ eV under study, the electrons may be concentrated to $\varnothing^{(1)}_{src.} \approx 0.8$ mm, which implies an estimated divergence $\Delta\beta^{(o)}_{cap.} = 16$ mrad according to Fig. 7. The substitute from Fig. 8, about 20% less in its width and 2.2 × farther from the RZP than the real sample, so equals virtually the étendue of 70 μm^2 from Eq. (3). Driven by the demand for a maximized efficiency with respect to acceptance angle and $(+1)^{st}$ order diffraction, and restricted by the largest feasible grating length L and line density $d_l \lesssim 2 \times 10^3\,mm^{-1}$ in electron beam lithography, our design follows the parameters listed in Tab. 3. The exit arm length R'_2 [3] and the grating's $c_{ff} \equiv \cos\beta_0/\cos\alpha_0$ are chosen to support

Optics EXPRESS

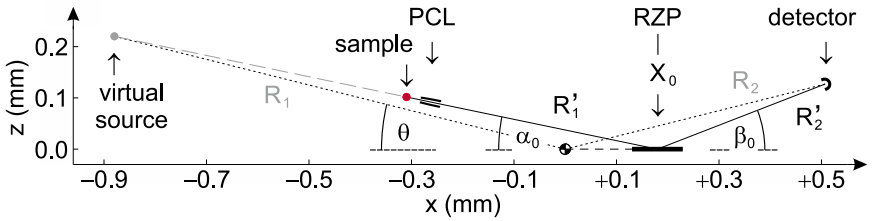

Fig. 8. Side view of the planned spectrometer in optical coordinates (Tab. 3). The real source equals the sample position (red dot) in a distance R'_1 from the RZP. Dashed / dotted lines correspond to the virtual source (gray dot), which is used for simulations.

Table 3. **Instrumental design parameters, according to Fig. 8**

ΔE [eV]	R'_1 [mm]	R'_2 [mm]	α_0	β_0	L [mm]
≤ 0.5	500	350	11.7°	21.2°	90
E_0 [eV]	R_1 [mm]	R_2 [mm]	θ		X_0 [mm]
36.0	907	522	14.1°		+180

these goals, to ensure a resolution $0.25\,\text{eV} \leq \Delta E \leq 0.5\,\text{eV}$ – whose lower limit is defined by the intrinsic spectral width of the injected electron beam – and to suppress mainly chromatic aberrations [20]. A plane Si substrate with an rms slope error of 0.5" (sag.) × 0.2" (mer.) should carry the laminar grating profile of the RZP, coated by an amorphous, 40 nm thick Carbon layer [21]. With an RCWA-optimized ("rigorous coupled wave analysis"), constant groove depth near 31 nm as sketched in Fig. 9, we estimate an intensity-weighted diffraction efficiency of 21.7% for the elliptical, 17.6 mm wide footprint of the collimated beam in the grating plane. Taking into account the solid angle of 4.5×10^{-2} [sr] under which the PCL captures the radiation, and its transmission $\langle T \rangle_{\Delta z}$, an overall fraction of 5×10^{-4} from the 2π emission is expected to constitute the signal.

Apart from the substrate roughness, the mounting is assumed to guarantee an rms precision of ±0.2" (pitch) and ±1.0" (roll/yaw) as well as a displacement tolerance up to ±2 μm. Misalignments of that magnitude have no impact on the simulated Gaussian focus FWHM, which measures $\lesssim 0.5\,\text{mm} \times 0.4\,\text{mm}$ (H × V), in its dispersive (V) dimension 1.8 × more than for a monochromatic source. The dispersion [20]

$$dE/dz_{\text{det.}} = -0.79\,\text{eV/mm} + O(z^2_{\text{det.}}) \quad \text{at} \quad E \approx E_0 \tag{4}$$

then provides a spectral resolution as depicted on the left in Fig. 10, where the ±1% range refers to a correspondingly varied spot size, e.g. caused by a slightly different energy spread of the electrons. For special applications, the emission from the sample may be enhanced at the expense of a larger spot $\varnothing^{(1)}_{\text{src.}}$. The resolution, plotted on the right of Fig. 10, nevertheless degrades to no more than ≈ 0.5 eV for an infinitely extended source. From the application's point of view, we emphasize the fact that ΔE is mainly determined by $\varnothing^{(1)}_{\text{src.}}$. In contrast, the resolution is robust with respect to the uncertainty in the output divergence $\Delta\beta^{(o)}_{\text{cap.}}$ as discussed in Sect. 3 and represented by the reliable function on the right in Fig. 7. In particular, the "full aperture" usage of the PCL, only simulated until now, would still enable a resolution of (0.26 ± 0.02) eV for $\varnothing^{(1)}_{\text{src.}} = 0.1$ mm. On the other hand, the functional behavior as shown on the right in Fig. 10 is maintained for a source size above 0.2 mm, nearly regardless the exploited PCL aperture size.

Optics EXPRESS

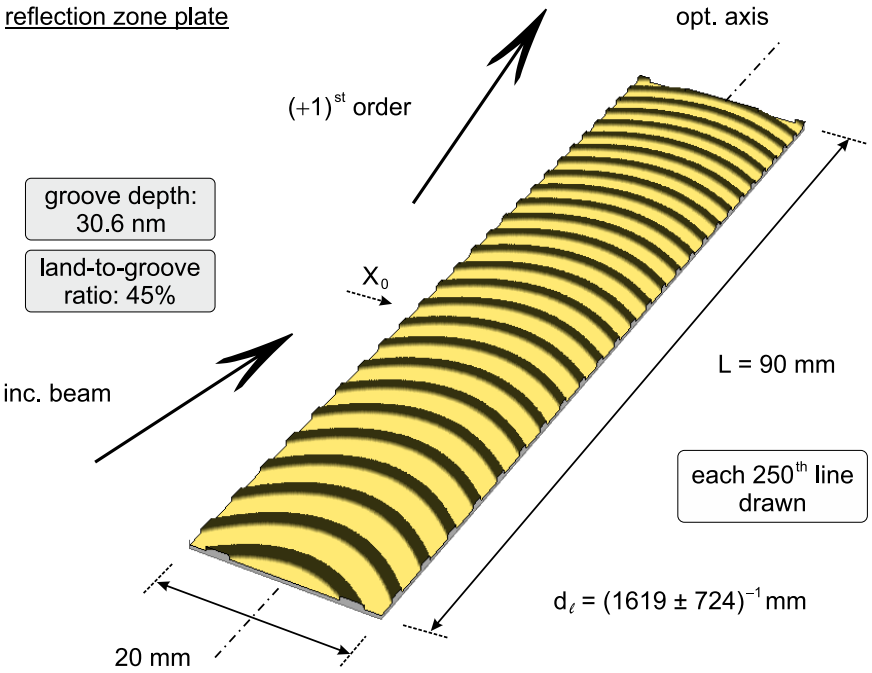

Fig. 9. Calculated laminar grating structure in true scale with respect to the lateral (x, y) dimensions. Lands are colored in black, grooves in yellow. Their constant profile parameters are optimized for maximal on-axis $(+1)^{st}$ order diffraction efficiency at the geometrical center X_0.

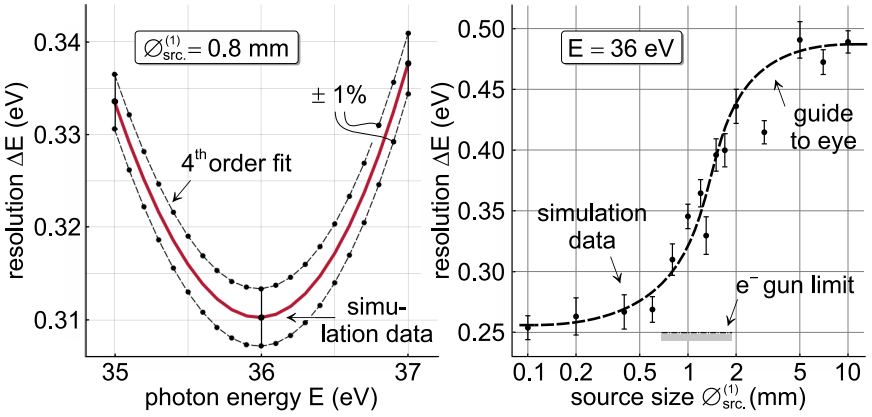

Fig. 10. Spectrometer resolution for the nominal source size of 0.8 mm (FWHM) on the left and for the design energy but a variable diameter of the emission region on the right, both simulated by ray tracing. The standard error budget for the grating (see text) is included.

5. Wideband soft X-ray spectrometry

Since the PCL has been tested comprehensively so far only at $E_0 = 36$ eV, i.e. the designated energy for this isochromat, the spectrometric use of the IPES instrument over a broad band of several eV is currently under investigation. As a first step toward this goal, we measure

Optics EXPRESS

the transmission of the PCL in the reflectometer (Sect. 2) up to an energy of 1.7 keV. The corresponding experimental results are shown in Fig. 11. Across the displayed energy range,

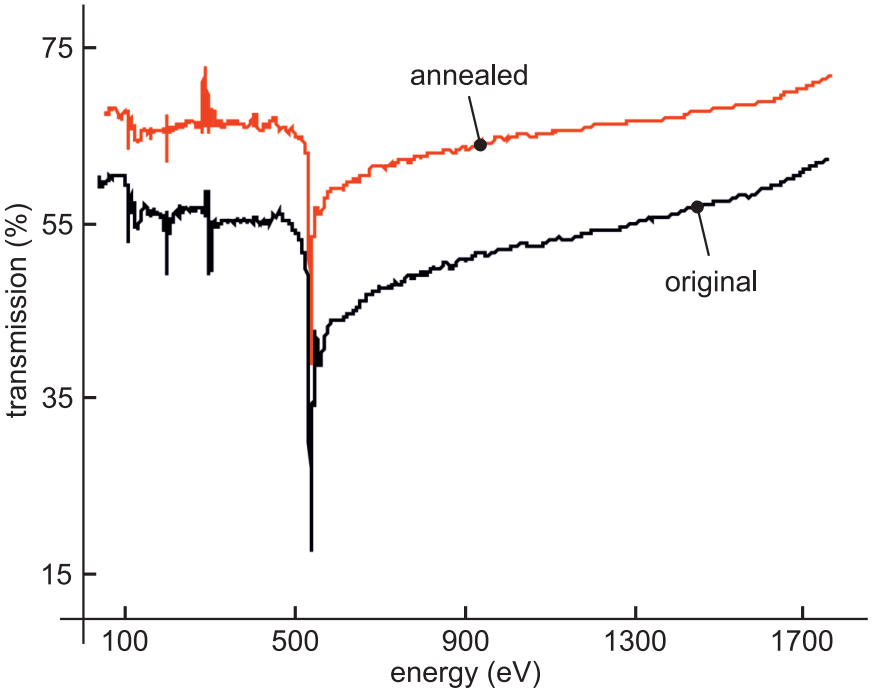

Fig. 11. Measured transmission of the polycapillary half lens between approximately 30 eV and 1750 eV, before (black) and after (red) an annealing procedure to remove dust etc.

emission lines and absorption edges of several elements, that constitute the borosilicate glass, arise as sharp peaks and dips, respectively. Among them, the Oxygen K edge at 0.53 keV represents the most prominent one. Annealing the material leads to an increase of the transmission by $\approx 10\%$ over the whole range, indicating the importance of a carefully cleaned inner and outer PCL aperture.

Anyway, let us assume that the capillary lens performs in the XUV independently from the wavelength – apart from the surface reflectivity which varies by less than 2% between e.g. 30 eV and 40 eV [13]. We also neglect the weak change $\Delta P^{(+1)}_{\mathrm{RZP}}$ of the grating diffraction efficiency of no more than about $\pm 1.3\%$ in that range. In this case, the dispersion and sufficiently low aberrations of the RZP would allow to replace the single channel detector (i.e. photo diode or channeltron) by an imaging-type detector, to cover a spectral band of up to $\sim 10\,\mathrm{eV}$. Ray tracing results, combined with the dispersion curve, are shown in Fig. 12. The simulation reveals a resolution

$$\Delta E = \sum_{n=0}^{4} c_n \, (E - E_0)^n \quad \text{for} \quad 30\,\mathrm{eV} \le E \le 40\,\mathrm{eV} \tag{5}$$

with $c_0 = 3.2 \times 10^{-1}\,\mathrm{eV}$ as the leading term for E_0 and higher order coefficients $c_1 = 5.0 \times 10^{-3}$, $c_2 = 2.6 \times 10^{-2}\,\mathrm{eV}^{-1}$, $c_3 = 5.6 \times 10^{-4}\,\mathrm{eV}^{-2}$ and $c_4 = -2.3 \times 10^{-4}\,\mathrm{eV}^{-3}$. Across an interval of 5.4 eV around E_0, Eq. (5) fulfills the desired limit $\Delta E \le 0.5\,\mathrm{eV}$ from Tab. 3, whereas a spectrum over the total range from $(30 - 40)\,\mathrm{eV}$ spreads to $\Delta z_{\mathrm{det.}} \lesssim 16\,\mathrm{mm}$.

Finally, we check the angular and positional RZP tolerance, required to maintain a resolution limit as listed in Tab. 4. Out of all dimensions, the z-related misalignment levels $\Omega^{(z)}_{\mathrm{yaw}}$ and $\Delta^{(z)}_{\mathrm{vertical}}$

Optics EXPRESS

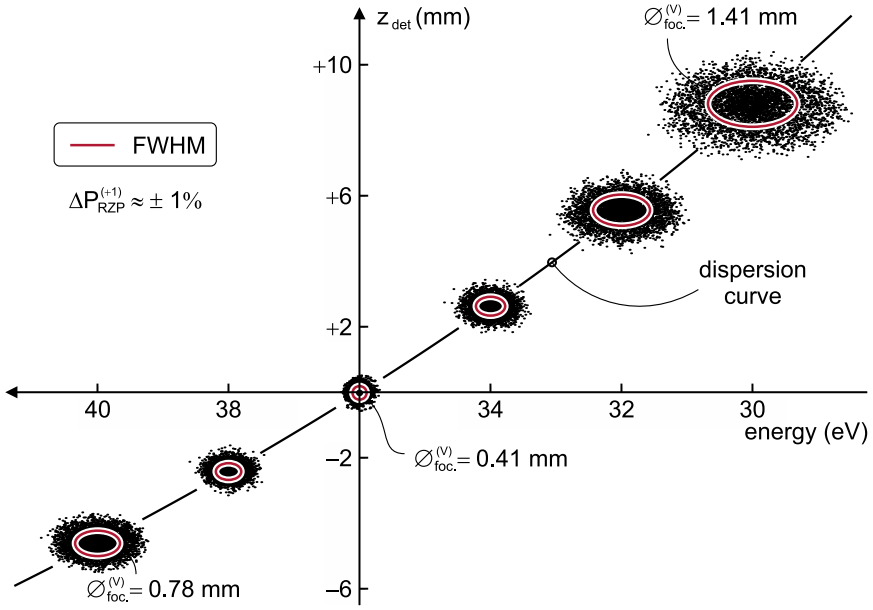

Fig. 12. Test spectrum around 36 eV as simulated by ray tracing (black dots), composed from 6 equidistant photon energies with an intrinsic bandwidth of 0.25 eV. Note that the spots are artificially displaced in the direction perpendicular to the $z_{\text{det.}}$ axis, to illustrate the dispersion function $z_{\text{det.}}(E)$. The spatial resolution is indicated by the FWHM ellipse (dark red curve).

Table 4. **Grating error budget in 6D for $\Delta E \leq 0.4\,\mathbf{eV}/0.5\,\mathbf{eV}$**

$\pm\Omega^{(x)}_{\text{roll}}$	$\pm\Omega^{(y)}_{\text{pitch}}$	$\pm\Omega^{(z)}_{\text{yaw}}$
$> 0.28°$	$\leq 0.04°/0.06°$	$\leq 0.02°/0.04°$
$\pm\Delta^{(x)}_{\text{longitudinal}}$	$\pm\Delta^{(y)}_{\text{lateral}}$	$\pm\Delta^{(z)}_{\text{vertical}}$
$\leq 0.6\,\text{mm}/1.0\,\text{mm}$	$> 2.0\,\text{mm}$	$\leq 0.3\,\text{mm}/0.4\,\text{mm}$

turn out as the most restrictive. Clearly, the compact and subcritical design without moving parts allows, in principle, for a relaxed mechanical precision of the grating mount well below the albeit still feasible arcsec regime from above.

6. Conclusion

In conclusion, the experimentally verified properties of a collimating polycapillary half lens in the XUV range are exploited to propose and design a powerful, compact, and flexible instrument for improved inverse photoemission spectroscopy around 36 eV. The sample radiation may be captured with a spatial resolution down to (0.3 ± 0.1) mm and a large numerical aperture (NA) up to 0.12. The low divergence of the collimated beam on the mrad scale will enable, together with a two-dimensional focusing reflection zone plate as the wavelength dispersive component, a spectral resolution of 0.3 eV. The collection efficiency of 5×10^{-4} under relaxed alignment constraints should allow for a stable and, compared to its capillary-free analogue with an elongated entrance arm, $14\times$ higher count rate in "single shot", i.e. stationary data acquisition without mechanical movements.

Next, the reflection zone plate will be fabricated by in-house facilities and the proposed instrument will be implemented in an UHV chamber at the Helmholtz-Zentrum Berlin für

Optics EXPRESS

Materialien und Energie GmbH. If realized successfully, our device is expected to keep up in its performance with commercially available versions of a capillary-based, table-top spectrometer (iMOXS®) provided by the Institute for Scientific Instruments GmbH in Berlin, though at an even lower energy.

We aim to decode the details how the radiation propagates through the tapered glass channels, confined to an angular divergence well below the critical angle of reflection, since our empirical findings, confirmed by elementary ray tracing, give clear evidence for a less complete theoretical understanding of the complex 3D image forming process in x-ray capillaries.

In future, consciously developed capillary lenses for that relatively long wavelength regime might provide an even increased aperture angle, transmission, and spatial resolution. Anyway, numerous exciting applications for this kind of focusing or collimating optics arise in the XUV: Achromatic in their nature – unlike diffractive zone plates and also in contrast to multilayer (Schwarzschild) mirror schemes, they are destined for broadband investigations, namely spectroscopy. If configured in a confocal scanning microscope, this important technique used in spatially resolved micro x-ray fluorescence analysis (μXRF) could be readily extended to the sub-keV emission lines of the lightest elements down to Be and Li $\lesssim 10^2$ eV.

Funding

Horizon 2020 Framework Programme (640868); Helmholtz Association (VH-NG-423).